This is the peer-reviewed, final accepted version for American Mineralogist, published by the Mineralogical Society of America.
The published version is subject to change. Cite as Authors (Year) Title. American Mineralogist, in press.
DOI: https://doi.org/10.2138/am-2023-9195. http://www.minsocam.org/

1 **Revision 1**

2 **4613 Words**

3 First widespread occurrence of rare phosphate chladniite in a meteorite, winonaite Graves
4 Nunataks (GRA) 12510: implications for phosphide – phosphate redox buffered genesis in
5 meteorites

6 **Brendan A. Anzures[1,2], Francis M. McCubbin[3], Timmons M. Erickson[2], Ryan S. Jakubek[2],**
7 **Marc D. Fries[3], Loan Le[2]**
8 [1]Lunar and Planetary Institute, USRA
9 [2]Jacobs, NASA Johnson Space Center
10 [3]ARES, NASA Johnson Space Center

Always consult and cite the final, published document. See http:/www.minsocam.org or GeoscienceWorld

This is the peer-reviewed, final accepted version for American Mineralogist, published by the Mineralogical Society of America.
The published version is subject to change. Cite as Authors (Year) Title. American Mineralogist, in press.
DOI: https://doi.org/10.2138/am-2023-9195. http://www.minsocam.org/

Revision 1

Abstract

The first widespread occurrence of rare Na-, Ca-, and Mg,Mn,Fe-bearing phosphate chladniite was observed in meteorite Graves Nunataks (GRA) 12510, which is a primitive achondrite that sits within the winonaite class. Numerous 1-500 μm chladniite grains were found, often on the margins between silicate clasts and the kamacite portions of the large metal veins that permeated through the sample. The largest chladniite grains are associated with merrillite, kamacite, taenite, troilite, albite, forsterite, diopside, and enstatite, with a few tiny chladniite grains and an apatite grain enclosed within merrillite. GRA 12510's average chladniite composition is $Na_{2.7}Ca_{1.25}(Mg_{10.02}Mn_{0.69}Fe_{0.20})_{\Sigma=10.91}(PO_4)_9$. Electron back scattered diffraction (EBSD) patterns indicate varying degrees of nucleation and growth of chladniite grains. Additionally, the first pure Raman spectrum of chladniite is described here revealing primary ν_1 bands at 954, 974, and especially 984 cm^{-1}. The co-occurrence and close association of merrillite, apatite, chladniite, and P-bearing metallic phases within GRA 12510 suggests that the fO_2 of IW-2 to IW-4 is an intrinsic property of the precursor chondritic material, and the phosphate-phosphide reaction may have buffered the final winonaite and IAB iron meteorite phase assemblages. Altogether, chladniite appears to form alongside other phosphates with their chemistries reflecting the diverse environment of their formation. Meteoritic chladniite likely formed through subsolidus oxidation of schreibersite, scavenging Na from albite, Ca from diopside, Mg from enstatite/forsterite, Fe from kamacite/taenite, and Mn from alabandite/chromite when available. A P^0-P^{5+} redox-buffered environment also has implications for thermometry and fast cooling rates, although more experiments are necessary to extrapolate powder reaction rates to those of larger crystals. Furthermore, phosphide-phosphate buffered experiments may aid in investigating equilibrium chemistry at fO_2's between IW-2 and IW-4,

Always consult and cite the final, published document. See http:/www.minsocam.org or GeoscienceWorld

This is the peer-reviewed, final accepted version for American Mineralogist, published by the Mineralogical Society of America.
The published version is subject to change. Cite as Authors (Year) Title. American Mineralogist, in press.
DOI: https://doi.org/10.2138/am-2023-9195. http://www.minsocam.org/

which have been challenging to explore experimentally due to the limited availability of solid metal-metal oxide buffers between IW (Fe-FeO) and IW-5 (Cr-Cr_2O_3) at temperatures and pressures relevant to planetary interiors. Future investigations of phosphide-phosphate redox-buffered genesis at fO_2's between IW-2 and IW-4 have important implications for *primitive meteorite constituents* (e.g. CAI's), *partially differentiated planetesimals*, and *planets* including Mercury and core formation on Earth.

Introduction

The winonaites are a small group of primitive achondrites that provide insights into the early differentiation and partial melting of chondritic planetesimals in the early Solar System (Benedix et al., 1998, 2005; Bild, 1977; Hunt et al., 2017, 2018; Zeng et al., 2019). Winonaites have not been studied in much detail since the discovery of their namesake Winona in 1928, although their number has more than doubled since 2020 from 33 to 82 through 2023 (Gattacceca et al., 2023). Winonaites are distinguished from other primitive achondrite groups based on their mineralogy and composition, reflecting reducing conditions intermediate between ordinary and enstatite chondrites (Benedix et al., 1998; Bild, 1977). Winonaites are also distinguished by their oxygen isotopic systematics that bear similarities to silicate inclusions in rare group IAB complex iron meteorites, implying they formed from the same parent body (Benedix et al., 1998; Bild, 1977). Winonaites are highly heterogeneous in grain size, petrologic texture, and modal minerology, reflecting a complex and varied geologic history (Benedix et al., 1998; Floss et al., 2007; Hunt et al., 2017; Li et al., 2011). Previous studies have revealed that winonaites experienced extensive thermal metamorphism, limited Fe-Ni-FeS partial melting, possible silicate partial melting, and catastrophic impact, breakup, and reassembly (Benedix et al., 1998, 2005; Bild, 1977; Floss et al., 2007; Hunt et al., 2017, 2018; Zeng et al., 2019; Anzures

Always consult and cite the final, published document. See http:/www.minsocam.org or GeoscienceWorld

This is the peer-reviewed, final accepted version for American Mineralogist, published by the Mineralogical Society of America.
The published version is subject to change. Cite as Authors (Year) Title. American Mineralogist, in press.
DOI: https://doi.org/10.2138/am-2023-9195. http://www.minsocam.org/

et al. 2022). Studies of winonaites and IAB iron meteorites have revealed several new minerals, including rare Na- and Mg-bearing phosphates chladniite (McCoy et al., 1994), moraskoite (Karwowski et al., 2015), and czochralskiite (Karwowski et al., 2016). Here, we describe the first widespread occurrence in a meteorite of the rare Mg-rich member of the fillowite-group chladniite ($Na_3CaMg_{11}(PO_4)_9$) (Hatert et al., 2011) and its first identification in a winonaite meteorite, Graves Nunataks (GRA) 12510 (Figure 1).

Phosphate minerals make up a minor to trace fraction of the modal mineralogy of most meteorite groups, and the most common phosphates in meteorites are apatite and merrillite (Jones et al., 2014, 2016; Mccubbin et al., 2023; McCubbin et al., 2021; McCubbin and Jones, 2015; Patiño Douce and Roden, 2006; Ward et al., 2017). Although they are minor phases, phosphates can provide invaluable insights into the petrogenesis of samples as they are often the primary carrier of rare earth elements (REE) (Pan and Fleet, 2002; Piccoli and Candela, 2002). Furthermore, some phosphates can host magmatic volatiles in their structure (i.e., F, Cl, and OH) and can provide insights into the volatile history of a sample, including the isotopic compositions of H and Cl (Barnes et al., 2019, 2020; Boyce et al., 2014; McCubbin and Ustunisik, 2018; Sarafian et al., 2017; Tartèse et al., 2019; Webster and Piccoli, 2015). For reduced systems, like the winonaites, phosphates can also provide important constraints on oxygen fugacity as the phosphate-phosphide transition occurs at about 4 log units below the iron-wüstite (IW) buffer (IW-4) at ~700 °C and at about IW-3 at ~1300 °C (Pasek, 2015). Very little is known about the phosphate mineral chladniite because it is rare in natural samples. Here we investigate the widespread occurrence of the fillowite-group mineral chladniite in winonaite GRA 12510 and its relation to the petrogenesis of GRA 12510.

Always consult and cite the final, published document. See http:/www.minsocam.org or GeoscienceWorld

This is the peer-reviewed, final accepted version for American Mineralogist, published by the Mineralogical Society of America.
The published version is subject to change. Cite as Authors (Year) Title. American Mineralogist, in press.
DOI: https://doi.org/10.2138/am-2023-9195. http://www.minsocam.org/

Sample Material

The polished thin section studied here, GRA 12510,5, was provided by the Astromaterials Acquisition and Curation Office at NASA's Johnson Space Center and was progressively polished down before a final finish with 50 nm colloidal silica dispersion. The thin section had a 20 nm carbon coat for electron probe microanalysis (EPMA) and scanning electron microscopy (SEM) elemental mapping, which was subsequently removed and recoated with a 5 nm carbon coat for electron backscatter diffraction (EBSD). The carbon coat was then polished off for Raman spectroscopy.

Analytical Methods

Electron probe microanalysis (EPMA)

Always consult and cite the final, published document. See http:/www.minsocam.org or GeoscienceWorld

This is the peer-reviewed, final accepted version for American Mineralogist, published by the Mineralogical Society of America.
The published version is subject to change. Cite as Authors (Year) Title. American Mineralogist, in press.
DOI: https://doi.org/10.2138/am-2023-9195. http://www.minsocam.org/

Phase identification and quantitative major and minor element chemistry measurements were completed using electron probe microanalysis (EPMA) using the JEOL 8530 field emission (FE) electron microprobe at NASA Johnson Space Center (JSC) using a ZAF correction. Silicate minerals were analyzed using a 15 kV accelerating voltage, a 10 nA beam current, and a 5 μm spot size via wavelength-dispersive X-ray spectroscopy (WDS). Metals and sulfides were analyzed using a 15 kV accelerating voltage, 20 nA beam current, and a 1-5 μm spot size. Natural and synthetic standards were used including canyon diablo troilite for S. Phosphates were analyzed using 15 kV accelerating voltage, 20 nA beam current, and 10 μm spot size. The analysis of phosphates, particularly apatite, followed procedures established and described in McCubbin et al., (2021). Natural and synthetic minerals were used as standards including SrF_2, albite, quartz, stikin anorthite, springwater olivine, Wilberforce apatite, ilmenite, and rhodonite (crystal setup LDE1: F, TAP (Na, Si, Al, Mg), PET (P, S), PETL (Cl, Ca, Ti), and LIFH (Fe, Mn). Individual EPMA analyses are included in the online supplementary files.

Scanning electron microscopy (SEM)

Modal mineralogy was calculated using elemental maps produced with the JEOL 7600 scanning electron microscope (SEM) at NASA JSC. Elemental maps were collected using an accelerating voltage of 15 kV, 20 nA beam current, and 8 mm working distance at a resolution of < 0.5 μm/pixel. Mineral phases were identified by the distribution of 16 elements (Na, Mg, Al, Si, P, S, K, Ca, Ti, Cr, Mn, Fe, Ni, Zn, C, O) along with energy-dispersive X-ray spectroscopy (EDS) spot analyses. Modal mineral abundances were determined by converting the elemental maps to mineralogical maps in XMapTools (Lanari et al., 2014, 2019) (Table 1, Figure 2).

Electron backscatter diffraction (EBSD)

Always consult and cite the final, published document. See http:/www.minsocam.org or GeoscienceWorld

This is the peer-reviewed, final accepted version for American Mineralogist, published by the Mineralogical Society of America.
The published version is subject to change. Cite as Authors (Year) Title. American Mineralogist, in press.
DOI: https://doi.org/10.2138/am-2023-9195. http://www.minsocam.org/

Quantitative phase indexing and microstructural maps of chladniite-bearing regions were collected using the JEOL 7900F FE-SEM at NASA JSC. Electron backscatter diffraction patterns (EBSPs) were collected using an Oxford Instruments Symmetry™ crystal metal oxide scintillator detector and an Oxford instruments Aztec 4.1 software package. Acquisition parameters included a 20 kV accelerating voltage, 10 nA beam current, ~20 mm working distance, and a 70° tilt relative to the beam incidence. Phosphate EBSPs were indexed using a fillowite match unit after the crystal structure of Araki and Moore (1981). In addition, a merrillite match unit based on the structural data of Xie et al. (2015) was included in all maps to identify additional phosphates and ensure accurate structural indexing of the grains. Maps were collected with a step size ranging from 0.5 - 0.2 μm.

Post-processing of the EBSD data used Oxford Instruments Aztec Crystal 2.2 program. All EBSD data were given a wild-spike noise reduction and a seven nearest neighbor zero-solution correction. An additional correction was applied to remove systematic misindexing of the fillowite data with disorientation relation of 180°<11-20> caused by mirror symmetry normal to the axis. Forescatter electron, EBSD phase and inverse pole figure (IPF) maps can be found in Figure 3. Fillowite pole plots are equal area, lower hemisphere projections.

Raman spectroscopy and Raman spectroscopic imaging

Chladniite and its associated minerals were measured using a WITec alph300R Raman microscope (XMB3000-3003) at NASA JSC. Both single spectra and a Raman image were collected. Incident 532 or 488 nm excitation was generated using a WITec diode laser (XSL3100-1154) producing ~170 μW or ~100 μW of incident power at the sample surface, respectively. For single spectral collections, the incident laser was focused on the sample surface using either a 100X magnification Zeiss EC Epiplan-Neofluar objective producing a 0.9 μm

Always consult and cite the final, published document. See http:/www.minsocam.org or GeoscienceWorld

This is the peer-reviewed, final accepted version for American Mineralogist, published by the Mineralogical Society of America.
The published version is subject to change. Cite as Authors (Year) Title. American Mineralogist, in press.
DOI: https://doi.org/10.2138/am-2023-9195. http://www.minsocam.org/

beam spot on the sample surface, or a 50X magnification Zeiss EC Epiplan objective producing a 1.2 μm spot size on the sample surface. The Raman scattered light was dispersed using a WITec UHTS600 (XMC3200-0600) spectrometer with a 300 g/mm grating, and the spectrum was detected using a back-illuminated, thermoelectrically cooled (-60^{o} C) CCD (XMC3022-1001). Single spectra were collected by averaging approximately 5-10 accumulations, each with a 10 second integration time. The Raman image of 100x100 spectra was collected over a 300x300 μm area of the sample for a Raman image resolution of 3 μm/pixel and a total of 10,000 individual spectra. The 50X magnification objective was used to collect the Raman image. The accumulation time for each individual Raman spectrum in the image was 5 seconds for an image accumulation time of 14 hours and 8 minutes. Principal component analysis (PCA) of the image was performed using WITec Project FIVE software to identify and map the main component minerals chladniite, merrillite, enstatite, diopside, olivine, and feldspar as shown in Figure 4a. Representative Raman spectra of chladniite and merrillite, as well as fillowite from the literature, are shown in Figure 4b.

Results

Occurrence

GRA 12510 is a coarse-grained winonaite with abundant metal veins and pools separating silicate clasts that are either dominated by orthopyroxene or orthopyroxene+olivine. Modal mineralogy is 65.43% silicate (28.27% orthopyroxene, 21.63% olivine, 4.54% clinopyroxene, and 10.87% plagioclase), 30.01% metal (26.08% kamacite, 3.50% taenite, and 0.43 % schreibersite), with minor troilite (2.73%), chromite (0.50%), merrillite (1.13%), chladniite (0.32%), and trace apatite (Table 1, Figure 2). Both silicate clast lithologies have similar silicate:metal area% ratios (84.33:8.15 and 85.11:10.77 for the orthopyroxene-rich and

Always consult and cite the final, published document. See http:/www.minsocam.org or GeoscienceWorld

This is the peer-reviewed, final accepted version for American Mineralogist, published by the Mineralogical Society of America.
The published version is subject to change. Cite as Authors (Year) Title. American Mineralogist, in press.
DOI: https://doi.org/10.2138/am-2023-9195. http://www.minsocam.org/

orthopyroxene + olivine-rich clasts). However, the orthopyroxene-rich clasts have more orthopyroxene (45.05 vs. 31.68%), less clinopyroxene (5.36 vs. 11.09%), similar abundances of plagioclase (12.85 vs. 11.64%), and less olivine (21.07 vs. 30.70%). A single 5 μm diameter grain of alabandite (MnS) was also found in an orthopyroxene-rich silicate clast in contact with troilite and schreibersite. A single F-rich, Cl-bearing apatite grain was found as an inclusion in merrillite. Notably, the orthopyroxene-rich clast has substantially more phosphate (0.67% chladniite and 1.66% merrillite vs. 0.31% chladniite and 1.23% merrillite) and less phosphide (0.09% vs. 0.81% schreibersite).

Numerous 1-500 μm chladniite grains were found, often on the margins between silicate clasts and the kamacite portions of the large metal veins. The largest chladniite grains are associated with merrillite, kamacite, taenite, troilite, albite, forsterite, diopside, and enstatite (Figure 2). Rarely, chladniite encloses <3 μm merrillite grains as seen in Figure 2b. Additionally, even though chladniite in this meteorite contains Mn, the areas immediately surrounding chladniite are mostly Mn-free. However, several Mn-rich chromite grains (7.89 wt% MnO) and one tiny alabandite grain (MnS) are found elsewhere in the section.

Composition of chladniite

The average composition of 37 analyses of 7 grains of chladniite in GRA 12510 is shown in Table 2. These chladniite grains include those near metal, merrillite, and silicates, as well as inclusions in merrillite and albite. Based on these analyses, the calculated mineral formula for chladniite in GRA 12510 is $Na_{2.7}Ca_{1.25}(Mg_{10.02}Mn_{0.69}Fe_{0.20})_{\Sigma=10.91}(PO_4)_9$ after Hatert et al. (2021)'s stoichiometry $Na_3CaMg_{11}(PO_4)_9$.

EBSD

Always consult and cite the final, published document. See http:/www.minsocam.org or GeoscienceWorld

This is the peer-reviewed, final accepted version for American Mineralogist, published by the Mineralogical Society of America.
The published version is subject to change. Cite as Authors (Year) Title. American Mineralogist, in press.
DOI: https://doi.org/10.2138/am-2023-9195. http://www.minsocam.org/

EBSD analyses of GRA 12510 revealed that the chladniite structure agreed well with fillowite (Araki and Moore, 1981) thus falling within the fillowite-type phosphate group. Chladniite areas were found using forescatter electron images (Figure 3). Diffraction patterns were collected from one large chladniite grain in area A, as well as chladniite areas with multiple grain boundaries in area A and B (areas A and B matching those identified in BSE images in Figure 1). The mean angular deviation values of the electron backscatter patterns for the maps ranged between 0.87 to 0.63 for fillowite-structure materials, corroborating the chladniite-type phosphate.

Crystallographic orientations displayed as IPP maps and pole plots showed a single 40 x 60 μm chladniite grain in area A (Figure 3a). Other chemically coherent chladniite areas including a 100 x 100 μm area (Figure 3b) and a ~500 μm diameter area (Figure 3c) were actually revealed through EBSD to be monomineralic granular aggregates with grain sizes down to 3 μm. The pole plots do not show a systematic pattern consistent with preferred growth orientation, rather with multiple random orientations, indicating nucleation and coalescence of grains (Prior et al., 1999).

Raman Spectroscopy

Here, the Raman spectra of pure chladniite is described for the first time revealing a diagnostic peak centered at 982 cm^{-1} as shown in Figure 4b. A previous attempt at collecting a Raman spectrum of chladniite in a type III silicate-phosphate (PG) inclusion in the Elga IIE iron meteorite resulted in a dominantly merrillite spectrum with a chladniite shoulder at 984 cm^{-1} (Litasov and Podgornykh, 2017). Phosphates typically have a main peak corresponding to the ν_1 symmetric stretching mode of PO_4^{3-} at 950-990 cm^{-1}, an antisymmetric ν_3 vibration at 1000-1175 cm^{-1}, as well as weaker bands due to the ν_2 bending mode at 400-500 cm^{-1}, ν_4 bending mode at

Always consult and cite the final, published document. See http:/www.minsocam.org or GeoscienceWorld

This is the peer-reviewed, final accepted version for American Mineralogist, published by the Mineralogical Society of America.
The published version is subject to change. Cite as Authors (Year) Title. American Mineralogist, in press.
DOI: https://doi.org/10.2138/am-2023-9195. http://www.minsocam.org/

550-640 cm^{-1}, and lattice modes at wavenumbers lower than 300 cm^{-1} (Litasov and Podgornykh, 2017). Chladniite appears to have three strong overlapping ν_1 bands at 954 cm^{-1}, 974 cm^{-1}, and 984 cm^{-1}, ν_3 bands at 1063, 1129, 1138, and 1154 cm^{-1}, ν_2 bands at 441 and 486 cm^{-1}, ν_4 bands at 563, 583, and 602 cm^{-1}, and lattice mode bands at 282 cm^{-1}. Although chladniite is isostructural with fillowite, the substitution of Mg for Mn^{2+} in chladniite affects the ν_1 vibrational frequencies. Fillowite has three ν_1 bands at 943, 959, and 974 cm^{-1} (RRUFF database) whereas chladniite shows ν_1 bands at 954, 974, and 984 cm^{-1}. Three strong overlapping ν_1 bands indicate that the PO_4 tetrahedra inhabit three non-equivalent positions with slight structural/environmental heterogeneity rather than a more uniform location in its crystal structure.

Discussion

Winonaite Parent Body Pressure-Temperature-Redox Conditions

There are some thermodynamic constraints on the formation conditions of the winonaite parent body that can be used to elucidate the formation of chladniite. The winonaite parent body has been estimated to be a small body with a radius of ~100 km (Benedix et al., 2005) that corresponds to a maximum pressure of 0.01 GPa (Lucas et al., 2020). The winonaite parent body is also fairly reduced, with silicates recording oxygen fugacities (fO_2) from IW-2.3 to IW-3.2 calculated using the FeO content of olivine (quartz-iron-fayalite) and pyroxene (quartz-iron-ferrosillite) (Benedix et al., 2005). In their study, Benedix et al. (2005) notes that that winonaite and IAB fO_2 estimates do not fall along any traditional metal-metal oxide buffers or the temperature and pressure dependent graphite-carbon monoxide buffer. However, this fO_2 range calculated from the silicates is consistent with the phosphide-phosphate oxidation transition of IW-3 to IW-4 designated by the schreibersite (Fe_3P)-whitlockite ($Ca_3(PO_4)_2$) buffer (Bindi et al., 2023; Pasek, 2015) as shown in Figure 5. Recent experiments also suggest that at temperatures

Always consult and cite the final, published document. See http:/www.minsocam.org or GeoscienceWorld

This is the peer-reviewed, final accepted version for American Mineralogist, published by the Mineralogical Society of America.
The published version is subject to change. Cite as Authors (Year) Title. American Mineralogist, in press.
DOI: https://doi.org/10.2138/am-2023-9195. http://www.minsocam.org/

225 >900 °C, the phosphide to phosphate reaction occurs rapidly with complete oxidation from
226 phosphide within a week and a few percent reduction of phosphate on the same timescale (Feng
227 and Pasek, 2023). The co-occurrence and close association of merrillite, chladniite, apatite, and
228 P-bearing metallic phases within GRA 12510 suggests that the fO_2 of IW-2 to IW-4 is an
229 intrinsic property of the precursor chondritic material and the phosphate-phosphide reaction may
230 have buffered the final winonaite and IAB iron meteorite phase assemblages.

231 The prevailing model for winonaite-IAB parent body formation is that it underwent
232 incomplete differentiation followed by catastrophic impact, breakup, and reassembly (Benedix et
233 al., 2000). Most recently, the proposed layered structure of the winonaite-IAB iron meteorite
234 parent body from the surface to the core was 1) precursor chondritic material, 2) diverse
235 lithologies that experienced limited metamorphism and FeNi-FeS partial melting, 3) residues of
236 silicate partial melting, and 4) incompletely differentiated molten metal represented by IAB iron
237 meteorites (Hunt et al., 2017; Zeng et al., 2019). Adding onto this model, winonaite and IAB iron
238 meteorites record rapid cooling rates of 0.48-1.75 °C/year, and therefore cooled from their peak
239 magmatic temperatures as collisional fragments during breakup prior to reassembly (Anzures et
240 al. 2022). Finally, the winonaite parent body also experienced multiple impact events that caused
241 liberation from the parent body before impacting and being found on Earth. Cosmic-ray exposure
242 ages for winonaites range from 0.02 to 0.08 Ga (Benedix et al., 1998), while IAB iron meteorites
243 range from 0.4 to 1.0 Ga (Voshage, 1967).

244 **Origin of Chladniite**

245 The only other occurrences of chladniite have been as a single large grain in a complex
246 silicate-bearing inclusion in IAB iron meteorite Carlton (McCoy et al., 1994), a minor phase in
247 lodranite GRA 95209 (Floss, 1999; Grew et al., 2010; McCoy et al., 2006; McCoy and Carlson,

Always consult and cite the final, published document. See http:/www.minsocam.org or GeoscienceWorld

This is the peer-reviewed, final accepted version for American Mineralogist, published by the Mineralogical Society of America.
The published version is subject to change. Cite as Authors (Year) Title. American Mineralogist, in press.
DOI: https://doi.org/10.2138/am-2023-9195. http://www.minsocam.org/

1998), as inclusions in merrillite-dominated phosphate aggregate in a IIE iron meteorite Elga (Litasov and Podgornykh, 2017), in a couple of terrestrial pegmatites in Argentina (Vallcorba et al., 2016) and Brazil (Hatert et al., 2021), and as a REE-bearing Y-chladniite in a granulite from Antarctica (Grew et al., 2006). The first terrestrial identification of chladniite was found in a pegmatite from Córdoba, Argentina, as up to 200 μm diameter inclusions in beusite, the Mn analog of the graftonite phosphate structural group (Vallcorba 2016). Based on chemical and textural evidence, the association of beusite and chladniite was interpreted as a replacement product of garnet during the magmatic stage (Vallcorba 2016) caused by destabilization of garnet due to phosphorous buildup (Colombo et al., 2012). Chladniite has also been found in another pegmatite in Sapucaia, Brazil (Hatert et al., 2021). Y-chladniite was also found in a granulite in Larsemann Hills, Antarctica as up to 250-1000 μm inclusions in fluorapatite associated with wagnerite, xenotime-(Y), monazite-(Ce), P-bearing K-feldspar, biotite, sillimanite, quartz, and pyrite. Y-chladniite was inferred to have formed at 800-860 °C and 0.6-0.7 GPa by reaction of biotite with an anatectic melt with phosphorous buildup by interaction with fluorapatite (Grew et al., 2006). However, terrestrial chladniite likely has a different mode of formation than meteoritic chladniite because of the much higher pressures and more oxidizing environments on Earth as well as the inferred differences in geological processes that occur on small asteroids versus the Earth's crust.

For meteoritic chladniite formation, two hypotheses for its formation are either as a 1) replacement product of a phosphate (either graftonite (Floss, 1999) or panethite (Litasov and Podgornykh, 2017), which originated by reaction of olivine and orthopyroxene with metallic iron containing P or 2) crystallization from the reaction of plagioclase and pyroxene with metallic iron or schreibersite (Floss, 1999). In lodranite GRA 95209, chladniite is also associated with a

Always consult and cite the final, published document. See http:/www.minsocam.org or GeoscienceWorld

This is the peer-reviewed, final accepted version for American Mineralogist, published by the Mineralogical Society of America.
The published version is subject to change. Cite as Authors (Year) Title. American Mineralogist, in press.
DOI: https://doi.org/10.2138/am-2023-9195. http://www.minsocam.org/

graftonite structural group phosphate in the iron analog graftonite as < 50 μm thick veins intersecting silicate phases adjacent to remnant metal or troilite (Floss, 1999). However, in IAB iron meteorite Carlton, the single chladniite grain (175 x 975 μm) is not associated with a graftonite group phosphate, rather with chlorapatite. In IIE iron meteorite Elga, chladniite was found in only one site as <10 μm inclusions in merrillite surrounded by schreibersite rims and enclosed within kamacite-taenite metal (Litasov and Podgornykh, 2017). In Elga, chladniite was suggested to be poorly crystalline due to its Raman spectra always being contaminated by merrillite peaks (Litasov and Podgornykh, 2017).

Chladniite in winonaite GRA 12510 is much more abundant and found in larger grain sizes here compared with other meteorites. Numerous 1-500 μm chladniite grains were found, often on the margins between silicate clasts and the kamacite portions of the large metal veins. The largest chladniite grains are associated with merrillite, kamacite, taenite, troilite, albite, forsterite, diopside, and enstatite (Figure 2). Additionally, unlike Elga where a few tiny poorly crystallized chladniite grains are included in merrillite (Litasov and Podgornykh, 2017), sometimes chladniite in GRA 12510 encloses <3 μm merrillite grains as seen in Figure 2b.

Chladniite compositions differ widely, which suggests that the composition is controlled by the geologic environment of formation rather than by crystal-chemical constraints (Vallcorba et al., 2016). Terrestrial pegmatitic chladniite has high Mn and Fe (13.96-14.42 wt% MnO and 15.98-17.37 wt% FeO) reflective of its pegmatitic environment (Hatert et al., 2021; Vallcorba et al., 2016) and association with Mn-phosphate beusite in Argentina (Vallcorba et al., 2016). Terrestrial granulite chladniite has similar Fe content (15.88 wt% FeO) but virtually no Mn (0.26 wt% MnO) due to its almost Mn-free environment (Grew et al., 2006). Lodranite GRA 95209's chladniite is also rich in Fe with a little less Mn (8.61 wt% MnO and 14.4 wt% FeO (Floss,

Always consult and cite the final, published document. See http:/www.minsocam.org or GeoscienceWorld

This is the peer-reviewed, final accepted version for American Mineralogist, published by the Mineralogical Society of America.
The published version is subject to change. Cite as Authors (Year) Title. American Mineralogist, in press.
DOI: https://doi.org/10.2138/am-2023-9195. http://www.minsocam.org/

1999)) reflective of its association with Fe-phosphate graftonite. Chladniite in silicate clasts of iron meteorites have very low Mn and Fe including IAB iron Carlton (0.30 MnO and 2.23 wt% FeO respectively) (McCoy et al., 1994) and IIE Elga (1.37 MnO and 5.11 wt% FeO) (Litasov and Podgornykh, 2017). GRA 12510's chladniite also has relatively low overall Mn and Fe (3.92 wt% MnO and 1.14 wt% FeO respectively). However, GRA 12510's chladniite is 10 times higher in Mn than in Carlton, which could have been scavenged from MnS or Mn-rich chromite that are spatially anticorrelated with abundant chladniite in the sample. Interestingly, this composition plots slightly within the proposed miscibility gap in a Fe^{2+}-Mn-Mg ternary for fillowite-type phosphates (Fransolet et al., 1998; Hatert et al., 2021) as shown in Figure 6. This possible miscibility gap has been hypothesized because of the larger difference in ionic radii between Mg and Mn compared with their similarities to Fe^{2+}, although this could also be due to small sample bias with only seven total occurrences of chladniite.

Altogether, chladniite appears to form alongside other phosphates with their chemistries reflecting the diverse environment of their formation. Meteoritic chladniite likely formed through subsolidus oxidation of schreibersite $(Fe,Ni)_3P$ scavenging Na from albite, Ca from diopside, Mg from enstatite/forsterite, Fe from kamacite/taenite, and Mn from alabandite/chromite when available. Near Mg-endmember enstatite and forsterite (Mg#>90) is generally the most abundant mineral aside from metal in winonaites, IAB irons, and lodranites, consistent with the Mg-, rather than Fe- or Mn-, endmember of the fillowite group being present in GRA 12510. Whereas Carlton likely formed in a Cl-rich environment with chlorapatite present (McCoy et al., 1994), and GRA 95209 forming in a Cl-poor and Fe-rich environment (Floss, 1999). Although Elga has both chladniite, merrillite, and schreibersite like GRA 12510, its silicates appear to be more oxidized with an average orthopyroxene composition of $En_{76}Fs_{21.5}Wo_{2.5}$. Elga's lower Mn in

Always consult and cite the final, published document. See http:/www.minsocam.org or GeoscienceWorld

This is the peer-reviewed, final accepted version for American Mineralogist, published by the Mineralogical Society of America.
The published version is subject to change. Cite as Authors (Year) Title. American Mineralogist, in press.
DOI: https://doi.org/10.2138/am-2023-9195. http://www.minsocam.org/

317 chladniite compared with GRA 12510 is also reflected in its Mn-poor chromite (2.15 wt% vs.
318 7.89 wt% MnO) and presence of only troilite rather than troilite and alabandite respectively.

319 **Implications**

320 This schreibersite-chladniite reaction appears to have buffered the redox state of GRA
321 12510 with the recorded fO_2 using FeO content of olivine (quartz-iron-fayalite) and pyroxene
322 (quartz-iron-ferrosillite) in winonaites/IAB iron meteorites (Benedix et al., 2005) corresponding
323 to the fO_2-T curve of the phosphide-phosphate buffer (Bindi et al., 2023; Pasek, 2015). The
324 primary texture of the schreibersite and secondary texture of the chladniite suggest that GRA
325 12510 was initially more reduced. Furthermore, within a single section of GRA 12510 studied
326 here, chladniite makes up a higher fraction of the modal mineralogy than schreibersite,
327 suggesting that this reaction was proceeding toward oxidation at the time of closure.
328 Schreibersite-chladniite and more broadly schreibersite-phosphate assemblages in other
329 meteorites including IAB iron Carlton, IIE iron Elga, lodranite GRA 95209, indicate they formed
330 in a P^0-P^{5+} redox-buffered environment with an oxygen fugacity of ~IW-3 to IW-4 dependent on
331 temperature.

332 A P^0-P^{5+} redox-buffered environment also has implications for thermometry and cooling
333 rates. Recent experiments found that at >900 °C (close to the closure temperatures of common
334 silicates such as clinopyroxene, orthopyroxene, and plagioclase), the phosphide to phosphate
335 reaction occurs rapidly with a few % oxidation from phosphide within days and complete
336 oxidation within a week, along with a few percent reduction of phosphate on the same timescale
337 (Feng and Pasek, 2023). These experiments using powdered reagents suggest that a phosphide-
338 phosphate phase assemblage would only be preserved if cooling rates were quite fast in the
339 presence of an available oxidant, much faster than the fastest cooling rates estimated for high-

Always consult and cite the final, published document. See http:/www.minsocam.org or GeoscienceWorld

This is the peer-reviewed, final accepted version for American Mineralogist, published by the Mineralogical Society of America.
The published version is subject to change. Cite as Authors (Year) Title. American Mineralogist, in press.
DOI: https://doi.org/10.2138/am-2023-9195. http://www.minsocam.org/

340 temperature meteorite equilibration at 10-100 °C/year for ordinary chondrites (Lucas et al.,
341 2020). However, those estimated cooling rates may not be a good analogy for the larger crystals
342 that are present in the interiors of asteroid parent bodies. Given that closure temperatures are
343 proportional to grain size squared (Dodson, 1973), grains twice as large will cool four times
344 more slowly for a given closure temperature. Therefore, to truly constrain cooling rates of
345 phosphide-phosphate phase assemblages, more experiments are needed to constrain solid-state
346 phosphide oxidation and phosphate reduction timescales for realistic grain sizes in meteorites.

Always consult and cite the final, published document. See http:/www.minsocam.org or GeoscienceWorld

This is the peer-reviewed, final accepted version for American Mineralogist, published by the Mineralogical Society of America.
The published version is subject to change. Cite as Authors (Year) Title. American Mineralogist, in press.
DOI: https://doi.org/10.2138/am-2023-9195. http://www.minsocam.org/

Furthermore, phosphide-phosphate buffered experiments may aid in investigating equilibrium chemistry at fO_2's between IW-2 and IW-4, which have been challenging to explore experimentally due to the limited availability of solid metal-metal oxide buffers between IW (Fe-FeO) and IW-5 (Cr-Cr_2O_3) at temperatures and pressures relevant to planetary interiors. This fO_2 range is of particular interest for understanding changes in S speciation that have been highlighted by (Brendan A. Anzures et al., 2020) where the dominant S species in silicate melt changes from FeS at fO_2 > IW-2 to MgS at fO_2 < IW-4, with a few experiments suggesting that CaS/Na_2S are the major species at IW-2 to IW-4. There is a growing recognition that such low fO_2 conditions (IW-2 to IW-4) were widespread and had a significant control on the formation of planetary bodies in the early solar system, including *primitive meteorite constituents* CAI's, type I CR chondrites, and CM refractory inclusions, *partially differentiated planetesimals* that sourced the winonaite-IAB iron, lodranite-acapulcoite, ureilite, IIE iron, and IIICD iron meteorites (Righter et al., 2016), and finally *planets* on the oxidized range for Mercury (IW-3 to IW-7) (McCubbin et al., 2012; Nittler et al., 2023; Zolotov et al., 2013) and reduced estimate for Earth's core formation (IW-2 to IW-3.5) (Badro et al., 2015; Dauphas, 2017; Fischer et al., 2017).

Acknowledgements

FMM acknowledges support from NASA's Planetary Science Research Program during this work. We are grateful to the Meteorite Working Group, now the Antarctic Meteorite Review Panel of the Astromaterials Allocation Review Board, for carefully evaluating our sample requests, and we thank the curatorial staff at NASA Johnson Space Center for allocation of the Antarctic meteorites used in this study. The U.S. Antarctic meteorite samples are recovered by the Antarctic Search for Meteorites (ANSMET) program which has been funded by NSF and

Always consult and cite the final, published document. See http:/www.minsocam.org or GeoscienceWorld

This is the peer-reviewed, final accepted version for American Mineralogist, published by the Mineralogical Society of America.
The published version is subject to change. Cite as Authors (Year) Title. American Mineralogist, in press.
DOI: https://doi.org/10.2138/am-2023-9195. http://www.minsocam.org/

NASA and characterized and curated by the Department of Mineral Sciences of the Smithsonian Institution and Astromaterials Acquisition and Curation Office at NASA Johnson Space Center, respectively.

References

Anzures, B.A., Dygert, N., and Lucas, M. (2022). Thermochemical evolution of the winonaite and IAB iron meteorite parent body. Proceedings of the 53rd Lunar and Planetary Science Conference, p. 2696. Lunar and Planetary Institute, Woodlands, TX.

Anzures, Brendan A., Parman, S. W., Milliken, R. E., Namur, O., Cartier, C., and Wang, S. (2020). Effect of Sulfur Speciation on Chemical and Physical Properties of Heavily Reduced Mercurian Melts. Geochimica et Cosmochimica Acta, 286, 1–18.

Araki, T., and Moore, P. B. (1981). Fillowite, Na 2 Ca (Mn, Fe) 7 2+(PO 4) 6: its crystal structure. American Mineralogist, 66.7-8, 827–842.

Badro, J., Brodholt, J. P., Piet, H., Siebert, J., and Ryerson, F. J. (2015). Core formation and core composition from coupled geochemical and geophysical constraints. Proceedings of the National Academy of Sciences, 112.40, 12310–12314.

Barnes, J. J., Franchi, I. A., McCubbin, F. M., and Anand, M. (2019). Multiple reservoirs of volatiles in the Moon revealed by the isotopic composition of chlorine in lunar basalts. Geochimica et Cosmochimica Acta, 266, 144–162.

Barnes, J. J., McCubbin, F. M., Santos, A. R., Day, J. M. D., Boyce, J. W., Schwenzer, S. P., Ott, U., Franchi, I. A., Messenger, S., Anand, M., and Agee, C. B. (2020). Multiple early-formed water reservoirs in the interior of Mars. Nature Geoscience, 13.4, 260–264.

Benedix, G. K., Lauretta, D. S., and McCoy, T. J. (2005). Thermodynamic constraints on the formation conditions of winonaites and silicate-bearing IAB irons. Geochimica et

Always consult and cite the final, published document. See http:/www.minsocam.org or GeoscienceWorld

This is the peer-reviewed, final accepted version for American Mineralogist, published by the Mineralogical Society of America.
The published version is subject to change. Cite as Authors (Year) Title. American Mineralogist, in press.
DOI: https://doi.org/10.2138/am-2023-9195. http://www.minsocam.org/

393 Cosmochimica Acta, 69.21, 5123–5131.
394 Benedix, G. K., McCoy, T. J., Keil, K., Bogard, D. D., and Garrison, D. H. (1998). A petrologic
395 and isotopic study of winonaites: Evidence for early partial melting, brecciation, and
396 metamorphism. Geochimica et Cosmochimica Acta, 62.14, 2535–2553.
397 Benedix, G. K., McCoy, T. J., Keil, K., and Love, S. G. (2000). A petrologic study of the IAB
398 iron meteorites: Constraints on the formation of the IAB-Winonaite parent body.
399 Meteoritics and Planetary Science, 35.6, 1127–1141.
400 Bild, R. W. (1977). Silicate inclusions in group IAB irons and a relation to the anomalous stones
401 Winona and Mt Morris (Wis). Geochemica et Cosmochemica Acta, 41, 1439–1456.
402 Bindi, L., Feng, T., and Pasek, M. A. (2023). Routes to reduction of phosphate by high-energy
403 events. Communications Earth and Environment, 4.1.
404 Boyce, J. W., Tomlinson, S. M., McCubbin, F. M., Greenwood, J. P., and Treiman, A. H. (2014).
405 The lunar apatite paradox. Science, 344.6182, 400–402.
406 Colombo, F., Sfragulla, J., and Del Tánago, J. G. (2012). The garnet - phosphate buffer in
407 peraluminous granitic magmas: A case study from pegmatites in the Pocho district,
408 Córdoba, Argentina. Canadian Mineralogist, 50.6, 1555–1571.
409 Dauphas, N. (2017). The isotopic nature of the Earth's accreting material through time. Nature,
410 541.7638, 521–524.
411 Feng, T., and Pasek, M. A. (2023). Thermal phosphide mineral oxidation chemistry. Proceedings
412 of the 54th Lunar and Planetary Science Conference, p. #1322. Lunar and Planetary
413 Institute, Woodlands, TX.
414 Fischer, R. A., Campbell, A. J., and Ciesla, F. J. (2017). Sensitivities of Earth's core and mantle
415 compositions to accretion and differentiation processes. Earth and Planetary Science

Always consult and cite the final, published document. See http:/www.minsocam.org or GeoscienceWorld

This is the peer-reviewed, final accepted version for American Mineralogist, published by the Mineralogical Society of America.
The published version is subject to change. Cite as Authors (Year) Title. American Mineralogist, in press.
DOI: https://doi.org/10.2138/am-2023-9195. http://www.minsocam.org/

Letters, 458, 252–262.

Floss, C. (1999). Fe,Mg,Mn-bearing phosphates in the GRA 95209 meteorite: Occurrences and mineral chemistry. American Mineralogist, 84.9, 1354–1359.

Floss, C., Jolliff, B. L., Benedix, G. K., Stadermann, F. J., and Reid, J. (2007). Hammadah al Hamra 193: The first amphibole-bearing winonaite. American Mineralogist, 92.4, 460–467.

Fransolet, A. M., Fontan, F., Keller, P., and Antenucci, D. (1998). La Serie johnsomervilleite-fillowite dans les associations de phosphates de pegmatites granitiques de l'Afrique Centrale. Canadian Mineralogist, 36, 355–366.

Gattacceca, J., McCubbin, F. M., Grossman, J. N., Schrader, D. L., Chabot, N. L., D'Orazio, M., Goodrich, C., Greshake, A., Gross, J., Joy, K. H., Komatsu, M., and Miao, B. (2023). The Meteoritical Bulletin, No. 111. Meteoritics and Planetary Science, 58.6, 901–904.

Grew, E. S., Armbruster, T., Medenbach, O., Yates, M. G., and Carson, C. J. (2006). Stornesite-(Y), (Y, Ca)□2Na6 (Ca,Na)8(Mg,Fe)43(PO4)36, the first terrestrial Mg-dominant member of the fillowite group, from granulite-facies paragneiss in the Larsemann Hills, Prydz Bay, East Antarctica. American Mineralogist, 91.8–9, 1412–1424.

Grew, E. S., Yates, M. G., Beane, R. J., Floss, C., and Gerbi, C. (2010). Chopinite-sarcopside solid solution,[(Mg, Fe) 3□](PO4) 2, in GRA95209, a transitional acapulcoite: Implications for phosphate genesis in meteorites. American Mineralogist, 95.2–3, 260–272.

Hatert, F., Grew, E. S., Vignola, P., Rotiroti, N., Nestola, F., Keller, P., Baijot, M., Bruni, Y., Fransolet, A. M., Dal Bo, F., and Depret, M. (2021). Crystal chemistry and nomenclature of fillowite-type phosphates. Canadian Mineralogist, 59.4, 781–796.

Hunt, A. C., Benedix, G. K., Hammond, S. J., Bland, P. A., Rehkämper, M., Kreissig, K., and Strekopytov, S. (2017). A geochemical study of the winonaites: Evidence for limited partial

Always consult and cite the final, published document. See http:/www.minsocam.org or GeoscienceWorld

This is the peer-reviewed, final accepted version for American Mineralogist, published by the Mineralogical Society of America.
The published version is subject to change. Cite as Authors (Year) Title. American Mineralogist, in press.
DOI: https://doi.org/10.2138/am-2023-9195. http://www.minsocam.org/

439 melting and constraints on the precursor composition. Geochimica et Cosmochimica Acta,
440 199, 13–30.
441 Hunt, A. C., Cook, D. L., Lichtenberg, T., Reger, P. M., Ek, M., Golabek, G. J., and
442 Schönbächler, M. (2018). Late metal–silicate separation on the IAB parent asteroid:
443 Constraints from combined W and Pt isotopes and thermal modelling. Earth and Planetary
444 Science Letters, 482, 490–500.
445 Jones, R. H., McCubbin, F. M., Dreeland, L., Guan, Y., Burger, P. V., and Shearer, C. K. (2014).
446 Phosphate minerals in LL chondrites: A record of the action of fluids during metamorphism
447 on ordinary chondrite parent bodies. Geochimica et Cosmochimica Acta, 132, 120–140.
448 Jones, R. H., McCubbin, F. M., and Guan, Y. (2016). Phosphate minerals in the H group of
449 ordinary chondrites, and fluid activity recorded by apatite heterogeneity in the Zag H3-6
450 regolith breccia. American Mineralogist, 101.11., 2452–2467.
451 Karwowski, Ł., Kryza, R., Muszyński, A., Kusz, J., Helios, K., Drożdżewski, P., and Galuskin,
452 E. V. (2016). Czochralskiite, Na4Ca3Mg(PO4)4, a second new mineral from the Morasko
453 IAB-MG iron meteorite (Poland). European Journal of Mineralogy, 28.5, 969–977.
454 Karwowski, Ł., Kusz, J., Muszyński, A., Kryza, R., Sitarz, M., and Galuskin, E. V. (2015).
455 Moraskoite, Na 2 Mg(PO 4)F, a new mineral from the Morasko IAB-MG iron meteorite
456 (Poland) . Mineralogical Magazine, 79.2, 387–398.
457 Lanari, P., Vho, A., Bovay, T., Airaghi, L., and Centrella, S. (2019). Quantitative compositional
458 mapping of mineral phases by electron probe micro-analyser. Geological Society Special
459 Publication, 478.1, 39–63.
460 Lanari, P., Vidal, O., De Andrade, V., Dubacq, B., Lewin, E., Grosch, E. G., and Schwartz, S.
461 (2014). XMapTools: A MATLAB©-based program for electron microprobe X-ray image

Always consult and cite the final, published document. See http:/www.minsocam.org or GeoscienceWorld

This is the peer-reviewed, final accepted version for American Mineralogist, published by the Mineralogical Society of America.
The published version is subject to change. Cite as Authors (Year) Title. American Mineralogist, in press.
DOI: https://doi.org/10.2138/am-2023-9195. http://www.minsocam.org/

processing and geothermobarometry. Computers and Geosciences, 62, 227–240.

Li, S., Wang, S., Bao, H., Miao, B., Liu, S., Coulson, I. M., Li, X., and Li, Y. (2011). The Antarctic achondrite, Grove Mountains 021663: An olivine-rich winonaite. Meteoritics and Planetary Science, 46.9, 1329–1344.

Litasov, K. D., and Podgornykh, N. M. (2017). Raman spectroscopy of various phosphate minerals and occurrence of tuite in the Elga IIE iron meteorite. Journal of Raman Spectroscopy, 48.11, 1518–1527.

Lucas, M. P., Dygert, N., Ren, J., Hesse, M. A., Miller, N. R., and McSween, H. Y. (2020). Evidence for early fragmentation-reassembly of ordinary chondrite (H, L, and LL) parent bodies from REE-in-two-pyroxene thermometry. Geochimica et Cosmochimica Acta, 290, 366–390.

McCoy, T. J., and Carlson, W. D. (1998). Opaque minerals in the GRA 95209 lodranite: A snapshot of metal segregation. Proceedings of the 29th Lunar and Planetary Science Conference, p. 1675. Lunar and Planetary Institute, Woodlands, TX.

McCoy, T. J., Carlson, W. D., Nittler, L. R., Stroud, R. M., Bogard, D. D., and Garrison, D. H. (2006). Graves Nunataks 95209: A snapshot of metal segregation and core formation. Geochimica et Cosmochimica Acta, 70.2, 516–531.

McCoy, T. J., Steele, I. M., Keil, K., Leonard, B. F., and Endress, M. (1994). Chladniite, Na2CaMg7 (PO4) 6: A new mineral from the Carlton (IIICD) iron meteorite. American Mineralogist, 79, 375–380.

McCubbin, F. M., and Jones, R. H. (2015). Extraterrestrial apatite: Planetary geochemistry to astrobiology. Elements, 11.3, 183–188.

Mccubbin, F. M., Lewis, J. A., Barnes, J. J., Boyce, J. W., Gross, J., Mccanta, M. C., Srinivasan,

Always consult and cite the final, published document. See http:/www.minsocam.org or GeoscienceWorld

This is the peer-reviewed, final accepted version for American Mineralogist, published by the Mineralogical Society of America.
The published version is subject to change. Cite as Authors (Year) Title. American Mineralogist, in press.
DOI: https://doi.org/10.2138/am-2023-9195. http://www.minsocam.org/

P., Anzures, B. A., Lunning, N. G., Elardo, S. M., Keller, L. P., Prissel, T. C., and Agee, C. B. (2023). On the origin of fluorine-poor apatite in chondrite parent bodies. American Mineralogist, 108, 1185–1200.

McCubbin, F. M., Lewis, J. A., Barnes, J. J., Elardo, S. M., and Boyce, J. W. (2021). The abundances of F, Cl, and H2O in eucrites: Implications for the origin of volatile depletion in the asteroid 4 Vesta. Geochimica et Cosmochimica Acta, 314, 270-293.

McCubbin, F. M., Riner, M. A., Vander Kaaden, K. E., and Burkemper, L. K. (2012). Is Mercury a volatile-rich planet? Geophysical Research Letters, 39.9, 1–5.

McCubbin, F. M., and Ustunisik, G. (2018). Experimental investigation of F and Cl partitioning between apatite and Fe-rich basaltic melt at 0 GPa and 950-1050 °C: Evidence for steric controls on apatite-melt exchange equilibria in OH-poor apatite. American Mineralogist, 103.9, 1455–1467.

Nittler, L. R., Boujibar, A., Crapster-Pregont, E., Frank, E. A., McCoy, T. J., McCubbin, F. M., Starr, R. D., Vorburger, A., and Weider, S. Z. (2023). Chromium on Mercury: New Results From the MESSENGER X-Ray Spectrometer and Implications for the Innermost Planet's geochemical evolution. Journal of Geophysical Research: Planets, e2022JE007691.

Pan, Y., and Fleet, M. E. (2002). Compositions of the apatite-group minerals: Substitution mechanisms and controlling factors. Phosphates: Geochemical, Geobiological and Materials Importance, 48, 13–50.

Pasek, M. A. (2015). Phosphorus as a lunar volatile. Icarus, 255, 18–23.

Patiño Douce, A. E., and Roden, M. (2006). Apatite as a probe of halogen and water fugacities in the terrestrial planets. Geochimica et Cosmochimica Acta, 70.12, 3173–3196.

Piccoli, P. M., and Candela, P. A. (2002). Apatite in igneous systems. Reviews in mineralogy

Always consult and cite the final, published document. See http:/www.minsocam.org or GeoscienceWorld

This is the peer-reviewed, final accepted version for American Mineralogist, published by the Mineralogical Society of America.
The published version is subject to change. Cite as Authors (Year) Title. American Mineralogist, in press.
DOI: https://doi.org/10.2138/am-2023-9195. http://www.minsocam.org/

and Geochemistry, 48.1, 255-292..

Prior, D. J., Boyle, A. P., Brenker, F., Cheadle, M. C., Austin, D., Lopez, G., Peruzzo, L., Potts, G. J., Reddy, S., Spiess, R., Timms, N. E., Trimby, P., Wheeler, J., and Zetterström, L. (1999). The application of electron backscatter diffraction and orientation contrast imaging in the SEM to textural problems in rocks. American Mineralogist, 84.11–12, 1741–1759.

Righter, K., Sutton, S. R., Danielson, L., Pando, K., and Newville, M. (2016). Redox variations in the inner solar system with new constraints from vanadium XANES in spinels. American Mineralogist, 101, 1928–1942.

Sarafian, A. R., John, T., Roszjar, J., and Whitehouse, M. J. (2017). Chlorine and hydrogen degassing in Vesta's magma ocean. Earth and Planetary Science Letters, 459, 311–319.

Tartèse, R., Anand, M., and Franchi, I. A. (2019). H and Cl isotope characteristics of indigenous and late hydrothermal fluids on the differentiated asteroidal parent body of Grave Nunataks 06128. Geochimica et Cosmochimica Acta, 266, 529–543.

Vallcorba, O., Casas, L., Colombo, F., Frontera, C., and Rius, J. (2016). First terrestrial occurrence of the complex phosphate chladniite: crystal-structure refinement by synchrotron through-the-substrate microdiffraction. European Journal of Mineralogy, 29.2, 287–293.

Voshage, H. (1967). Bestrahlungsalter und Herkunft der Eisenmeteorite. Zeitschrift Fur Naturforschung - Section A Journal of Physical Sciences, 22.4, 477–506.

Ward, D., Bischoff, A., Roszjar, J., Berndt, J., and Whitehouse, M. J. (2017). Trace element inventory of meteoritic Ca-phosphates. American Mineralogist, 102.9, 1856–1880.

Webster, J. D., and Piccoli, P. M. (2015). Magmatic apatite: A powerful, yet deceptive, mineral. Elements, 11.3, 177–182.

Always consult and cite the final, published document. See http:/www.minsocam.org or GeoscienceWorld

Xie, X., Yang, H., Gu, X., and Downs, R. T. (2015). Chemical composition and crystal structure of merrillite from the Suizhou meteorite. American Mineralogist, 100.11–12, 2753–2756.

Zeng, X., Shang, Y., Li, S., Li, X., Wang, S., and Li, Y. (2019). The layered structure model for winonaite parent asteroid implicated by textural and mineralogical diversity. Earth, Planets and Space, 71.1, 1-15.

Zolotov, M. Y., Sprague, A. L., Hauck, S. A., Nittler, L. R., Solomon, S. C., and Weider, S. Z. (2013). The redox state, FeO content, and origin of sulfur-rich magmas on Mercury. Journal of Geophysical Research: Planets, 118.1, 138–146.

Figure Captions

Figure 1. BSE image of two areas ((**a**) area A and (**b**) area B) of chladniite with associated minerals merrillite, kamacite, taenite, troilite, albite, forsterite, diopside, and enstatite.

Figure 2. Mineralogical map of GRA 12510. Chladniite grains from 1-200 μm are scattered throughout the section often on margins between silicate clasts and metal. The areas immediately surrounding chladniite are mostly Mn-free, but several Mn-rich chromite grains (7.89 wt% MnO) and one tiny alabandite grain (MnS) are found elsewhere in the section. Schreibersite is also anti-correlated with chladniite. Black box insets correspond to areas A and B in figure 1. White circles are 75-150 μm LA-ICP-MS pits from previous trace element analyses.

Figure 3. EBSD data of three occurrences of chladniite ((**a**) area A, (**b**) area A, (**c**) area B) and its associated mineral assemblages with forward scattered electron diode (FSD), phase overlay, and inverse pole (IPF) images along with the Kikuchi patterns, Kikuchi bands, and Kikuchi solutions as well as pole figures {0001}, {10-10}, and {11-20}.

Figure 4. (**a**) Raman image overlaying an optical microscope image exhibiting the distribution of chladniite and merrillite in area B of GRA 12510. (**b**) Raman spectra of chladniite compared with merrillite and fillowite (RRUFF ID: R110143).

Figure 5. Plot of oxygen fugacity (log fO_2) vs. temperature (10000/T(K)) for IAB irons and a winonaite along with appropriate oxygen fugacity buffers adapted from Benedix et al. (2005). Oxygen fugacity determined from orthopyroxene (blue) and olivine (red) for meteorites Cad (Caddo County), CdC (Campo del Cielo), Cop (Copiapo), Lue (Lueders), Ude (Udei Station), Win (Winona) with data falling along the dashed best fit line. Winonaite and IAB iron meteorite oxygen fugacities fall along the schreibersite (Fe_3P) – whitlockite ($Ca_3(PO_4)_2$) buffer purple line (Pasek 2015; Bindi et al. 2023) indicating these meteorites were likely redox buffered by the

Always consult and cite the final, published document. See http:/www.minsocam.org or GeoscienceWorld

This is the peer-reviewed, final accepted version for American Mineralogist, published by the Mineralogical Society of America.
The published version is subject to change. Cite as Authors (Year) Title. American Mineralogist, in press.
DOI: https://doi.org/10.2138/am-2023-9195. http://www.minsocam.org/

present phase assemblage of phosphide (P valence state of 0) and phosphate (P valence state of 5+). Also shown are three CO-C fugacity buffers at different pressures that fall on a different slope.

Figure 6. Ternary Fe^{2+}-Mn-Mg diagram of natural fillowite-type phosphates. The most Mn-rich analysis of chladniite in GRA 12510 falls slightly within the proposed miscibility gap of Hatert et al. (2021).

Always consult and cite the final, published document. See http:/www.minsocam.org or GeoscienceWorld

This is the peer-reviewed, final accepted version for American Mineralogist, published by the Mineralogical Society of America.
The published version is subject to change. Cite as Authors (Year) Title. American Mineralogist, in press.
DOI: https://doi.org/10.2138/am-2023-9195. http://www.minsocam.org/

Revision 1

Table 1. Modal abundance of minerals in GRA 12510 (by area %)

enstatite	27.89
diopside	4.10
albite	11.49
forsterite	20.04
chromite	0.83
kamacite	25.92
taenite	4.54
schreibersite	1.09
troilite	2.88
alabandite	Trace
chladniite	0.78
merrillite	0.45
apatite	Trace

Table 2. Average major element compositions (wt%) of phosphates (chladniite, merrillite, and apatite), silicates and oxides (forsterite, enstatite, diopside, albite, and chromite), metals (kamacite, taenite, schreibersite), and sulfides (troilite, alabandite) in GRA 12510 from EPMA

Phosphates					
wt%	**chladniite**	**merrillite**	**apatite**		
SiO_2	0.25 (16)	*b.d.*	*b.d.*		
TiO_2	0.03 (00)	*b.d.*	*b.d.*		
FeO	1.14 (10)	0.32 (30)	0.75		
MnO	3.92 (12)	0.19 (3)	0.16		
MgO	32.58 (26)	3.78 (6)	0.13		
CaO	5.62 (3)	46.23 (21)	53.57		
Na_2O	6.75 (5)	2.75 (3)	0.08		
P_2O_5	51.22 (25)	47.14 (39)	42.02		
F[a]			2.38		
Cl			2.51		
S			0.01		
-O = F + Cl + S			1.65		
Total	101.51 (31)	100.42 (33)	99.96		
N	**37**	**20**	**1**		
Silicates and Oxides					
wt%	**forsterite**	**enstatite**	**diopside**	**albite**	**chromite**
SiO_2	42.06 (21)	59.95 (9)	54.91 (20)	65.55 (52)	0.02 (1)
TiO_2	*b.d.*	0.02 (0)	0.68 (4)	0.04 (1)	0.20 (6)
Al_2O_3	*b.d.*	0.03 (0)	0.81 (6)	21.38 (17)	0.46 (47)
Cr_2O_3					70.38 (52)

Always consult and cite the final, published document. See http:/www.minsocam.org or GeoscienceWorld

This is the peer-reviewed, final accepted version for American Mineralogist, published by the Mineralogical Society of America.
The published version is subject to change. Cite as Authors (Year) Title. American Mineralogist, in press.
DOI: https://doi.org/10.2138/am-2023-9195. http://www.minsocam.org/

FeO	3.11 (84)	0.48 (2)	1.06 (14)	0.29 (17)	13.77 (64)
MnO	0.97 (31)	0.24 (0)	0.36 (3)	0.01 (1)	7.89 (79)
MgO	55.51 (92)	40.18 (0)	18.73 (17)	0.01 (1)	6.05 (16)
CaO	0.02 (1)	0.65 (13)	22.09 (26)	2.38 (22)	0.01 (1)
Na_2O	*b.d.*	0.01 (1)	0.72 (5)	9.89 (16)	
V_2O_3					0.40 (13)
ZnO					1.30 (4)
Total	101.67	101.55	99.36	99.56	100.48
N	4	2	6	12	13
Metals and sulfides					
wt%	**kamacite**	**taenite**	**schreibersite**	**troilite**	**alabandite**
S	*b.d.*	*b.d.*		36.16 (71)	36.80 (10)
P	0.04 (2)	0.01 (1)	15.02 (4)	0.01 (1)	
Si	0.02 (1)	0.02 (2)	0.01 (0)	0.04 (1)	0.03 (2)
Mg	0.01 (1)	*b.d.*		0.02 (1)	0.02 (1)
Ca	0.01 (1)	0.01 (1)		0.07 (5)	0.01 (1)
Mn	0.01 (1)	*b.d.*		0.02 (2)	58.03 (29)
Ni	6.17 (34)	25.34 (70)	48.28 (71)	0.02 (2)	0.14 (6)
Cr	*b.d.*	*b.d.*		0.06 (2)	*b.d.*
Mo	*b.d.*	0.01 (1)		*b.d.*	*b.d.*
Fe	93.59 (133)	75.63 (63)	36.73 (60)	62.36 (52)	4.81 (19)
Co	0.55 (2)	0.25 (2)	0.11 (1)	0.08 (1)	
Total	100.42 (140)	101.29 (23)	100.14 (40)	98.84 (92)	99.83 (32)
N	29	5	20	7	5

[a]*X*-site sum exceeded 1 structural formula unit so F was computed assuming $X_F = 1 - X_{Cl}$ using the methods outlined in McCubbin et al., (2021)
N – number of analyses
b.d. – abundance was below detection limit
All parenthetical values represent 1-sigma standard deviation of the mean

Always consult and cite the final, published document. See http:/www.minsocam.org or GeoscienceWorld

This is the peer-reviewed, final accepted version for American Mineralogist, published by the Mineralogical Society of America.
The published version is subject to change. Cite as Authors (Year) Title. American Mineralogist, in press.
DOI: https://doi.org/10.2138/am-2023-9195. http://www.minsocam.org/

Figure 1

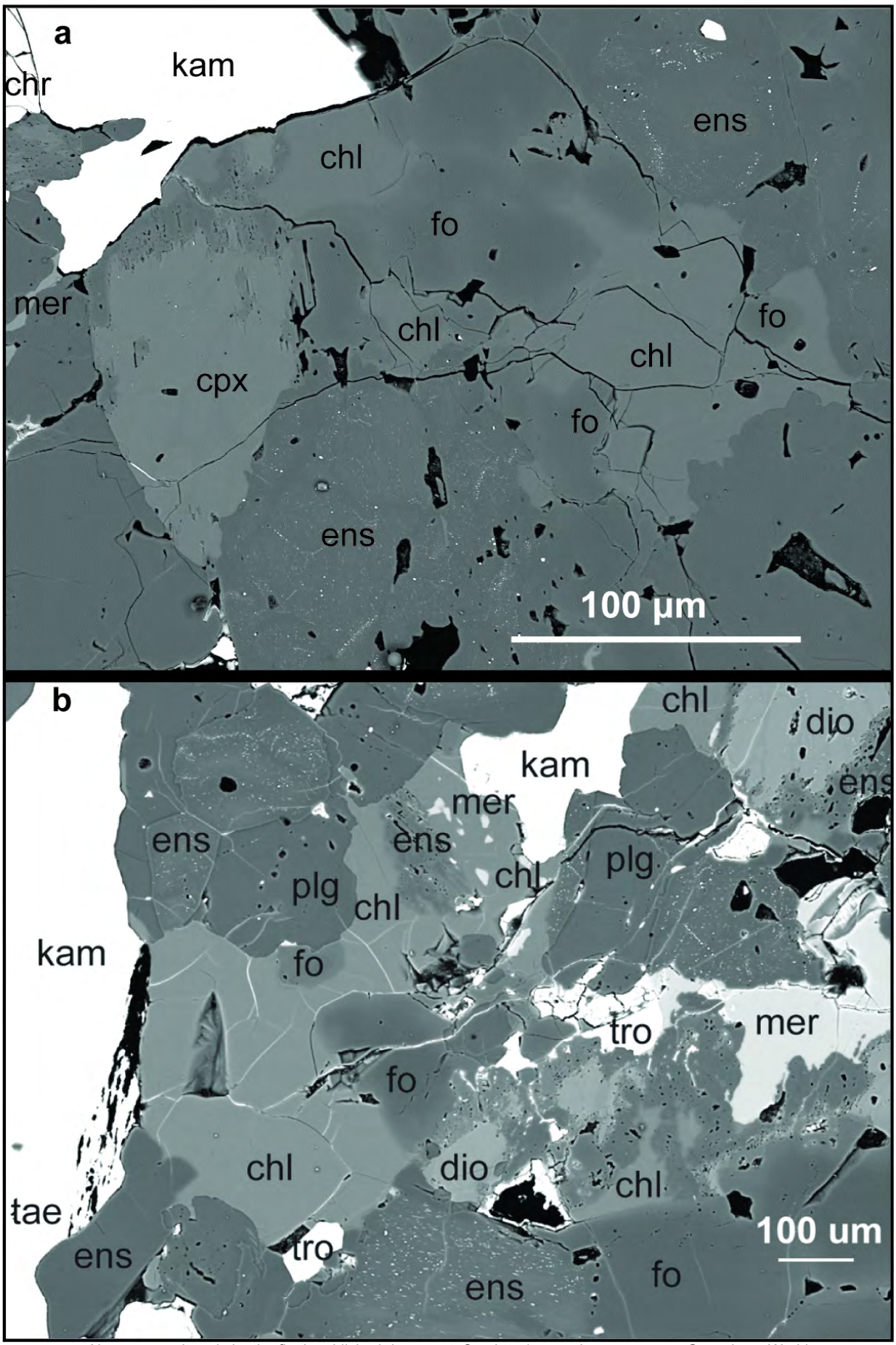

Always consult and cite the final, published document. See http:/www.minsocam.org or GeoscienceWorld

This is the peer-reviewed, final accepted version for American Mineralogist, published by the Mineralogical Society of America.
The published version is subject to change. Cite as Authors (Year) Title. American Mineralogist, in press.
DOI: https://doi.org/10.2138/am-2023-9195. http://www.minsocam.org/

Figure 2

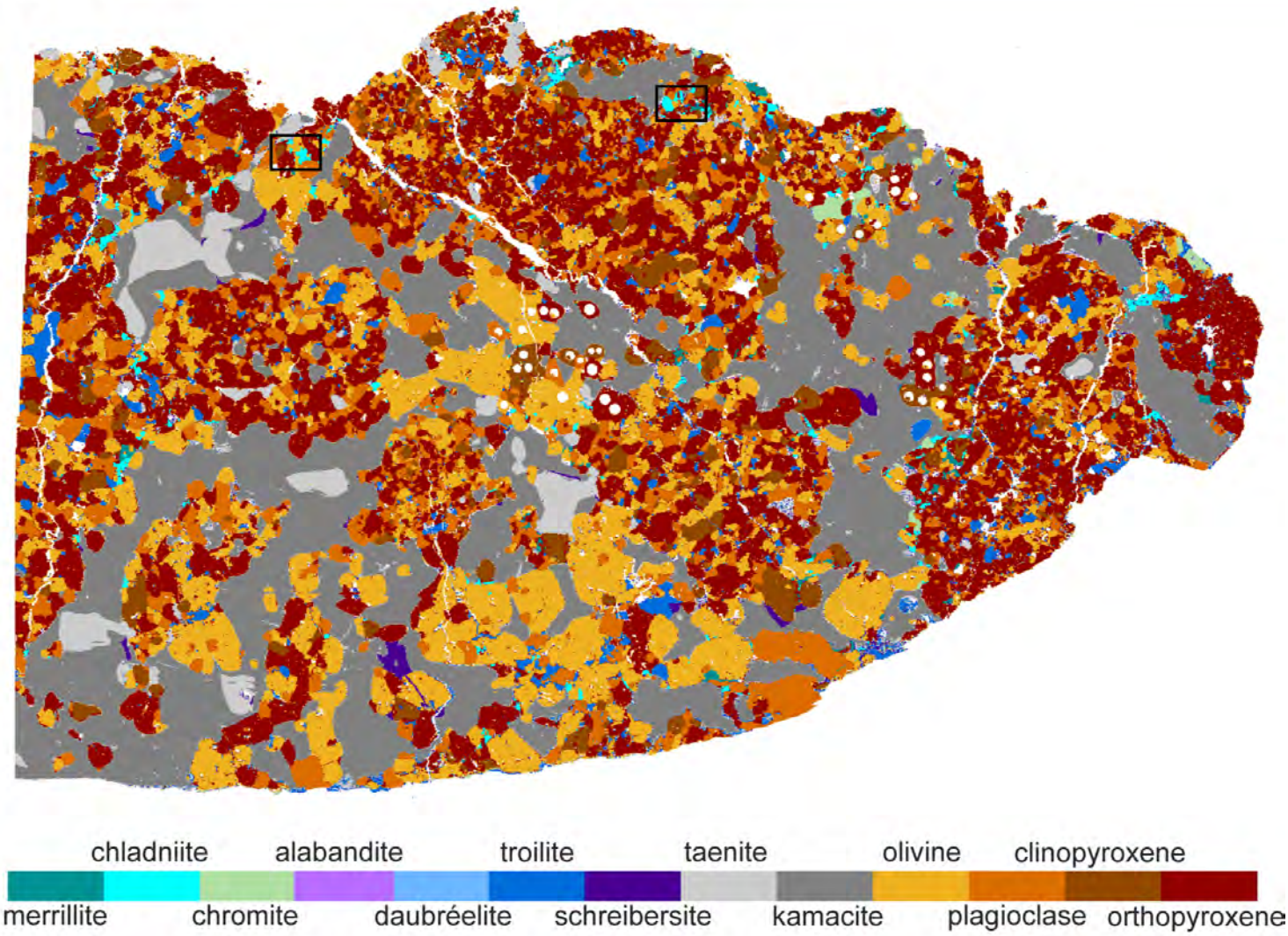

Always consult and cite the final, published document. See http:/www.minsocam.org or GeoscienceWorld

This is the peer-reviewed, final accepted version for American Mineralogist, published by the Mineralogical Society of America.
The published version is subject to change. Cite as Authors (Year) Title. American Mineralogist, in press.
DOI: https://doi.org/10.2138/am-2023-9195. http://www.minsocam.org/

Figure 3a

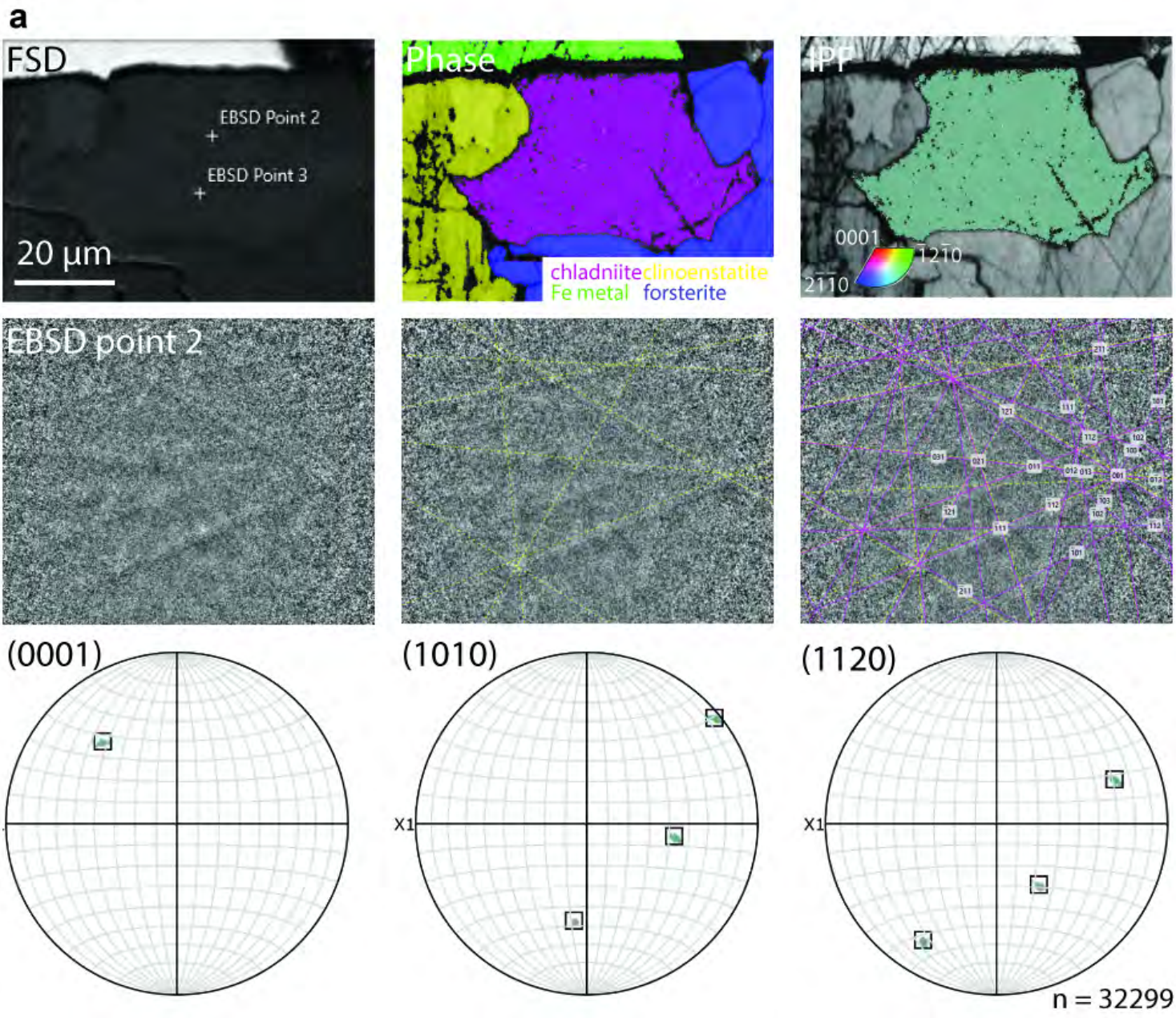

Always consult and cite the final, published document. See http:/www.minsocam.org or GeoscienceWorld

This is the peer-reviewed, final accepted version for American Mineralogist, published by the Mineralogical Society of America.
The published version is subject to change. Cite as Authors (Year) Title. American Mineralogist, in press.
DOI: https://doi.org/10.2138/am-2023-9195. http://www.minsocam.org/

Figure 3b

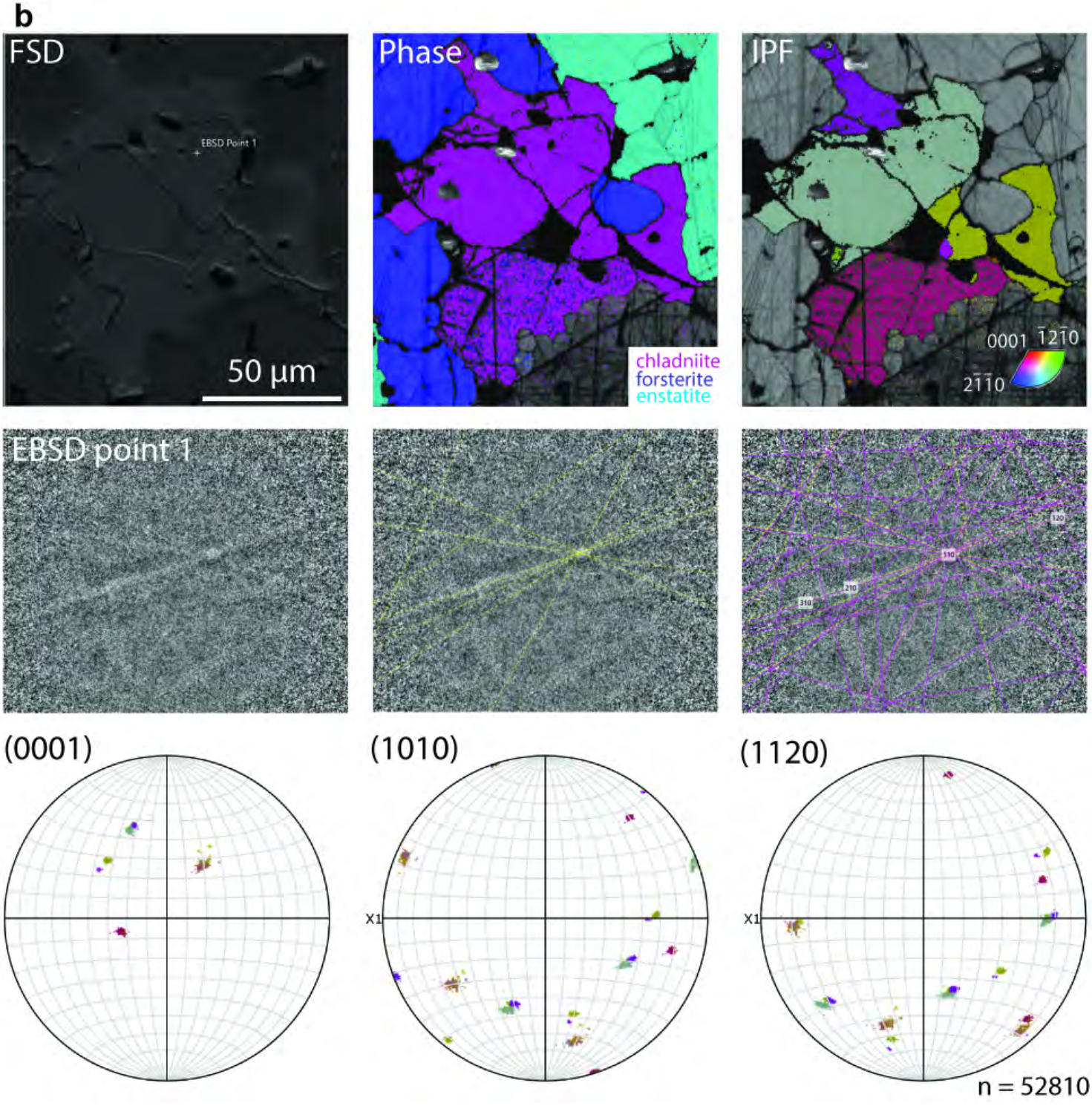

Always consult and cite the final, published document. See http:/www.minsocam.org or GeoscienceWorld

This is the peer-reviewed, final accepted version for American Mineralogist, published by the Mineralogical Society of America.
The published version is subject to change. Cite as Authors (Year) Title. American Mineralogist, in press.
DOI: https://doi.org/10.2138/am-2023-9195. http://www.minsocam.org/

Figure 3c

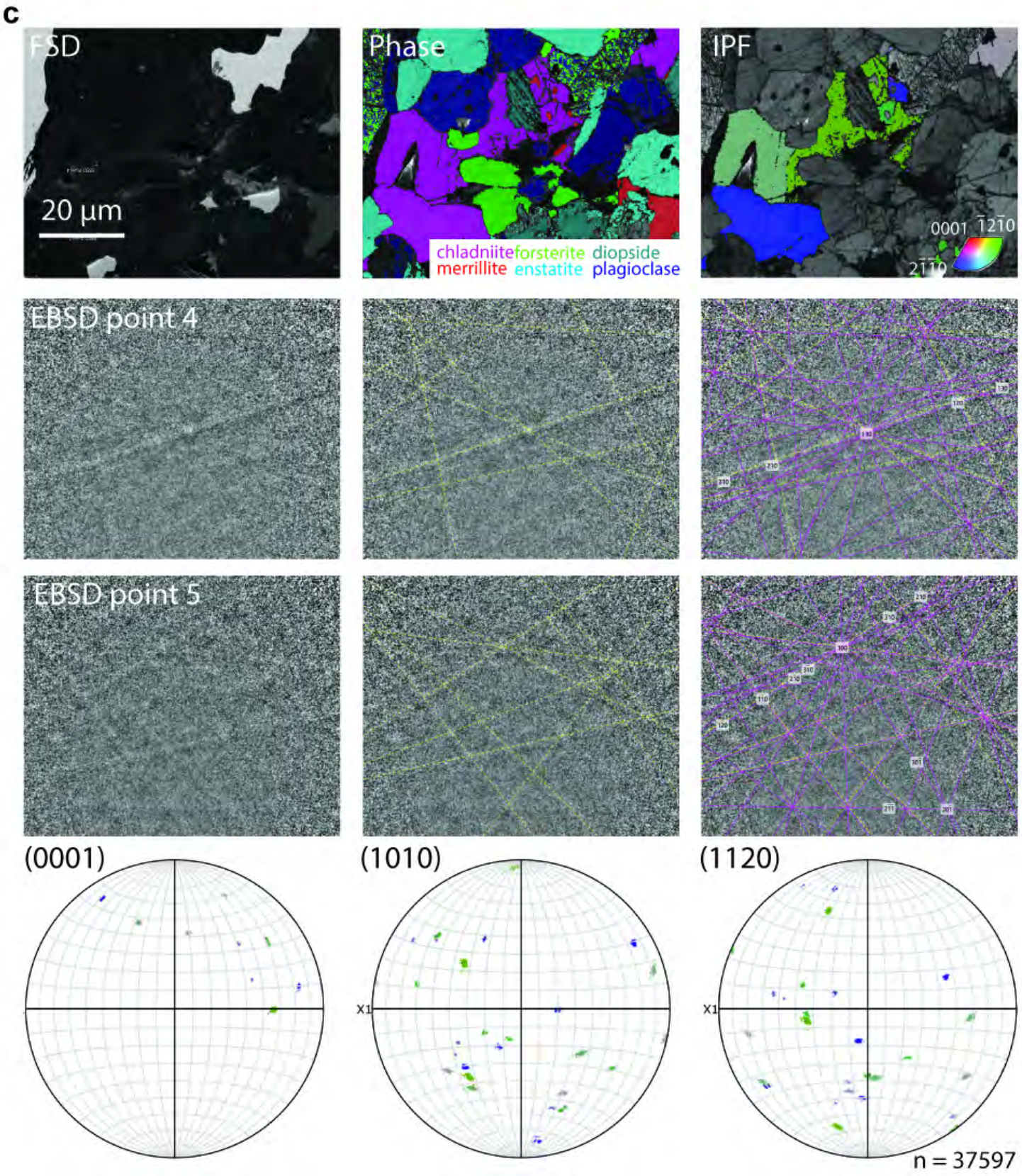

Always consult and cite the final, published document. See http:/www.minsocam.org or GeoscienceWorld

This is the peer-reviewed, final accepted version for American Mineralogist, published by the Mineralogical Society of America.
The published version is subject to change. Cite as Authors (Year) Title. American Mineralogist, in press.
DOI: https://doi.org/10.2138/am-2023-9195. http://www.minsocam.org/

Figure 4

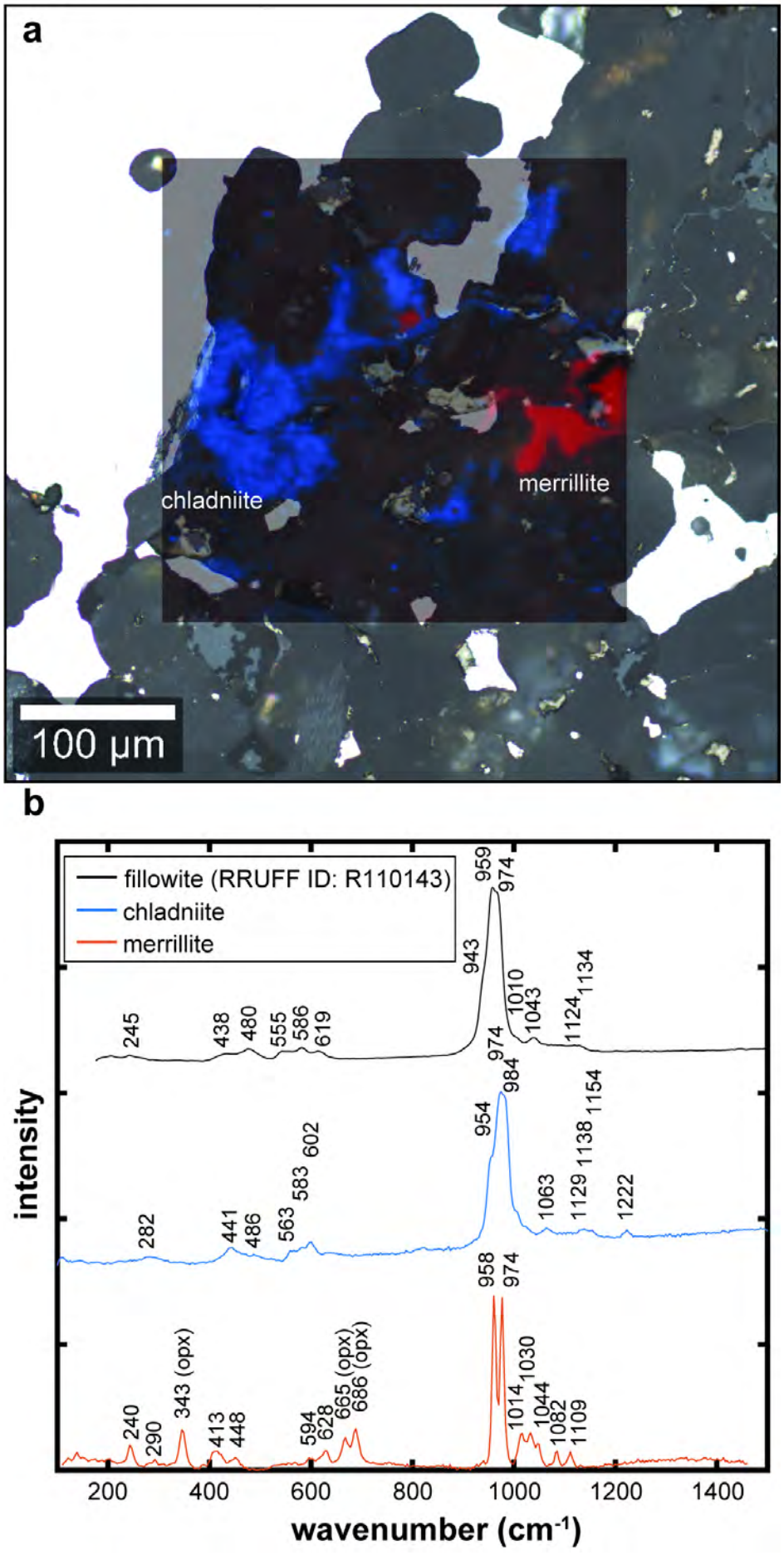

Always consult and cite the final, published document. See http:/www.minsocam.org or GeoscienceWorld

This is the peer-reviewed, final accepted version for American Mineralogist, published by the Mineralogical Society of America.
The published version is subject to change. Cite as Authors (Year) Title. American Mineralogist, in press.
DOI: https://doi.org/10.2138/am-2023-9195. http://www.minsocam.org/

Figure 5

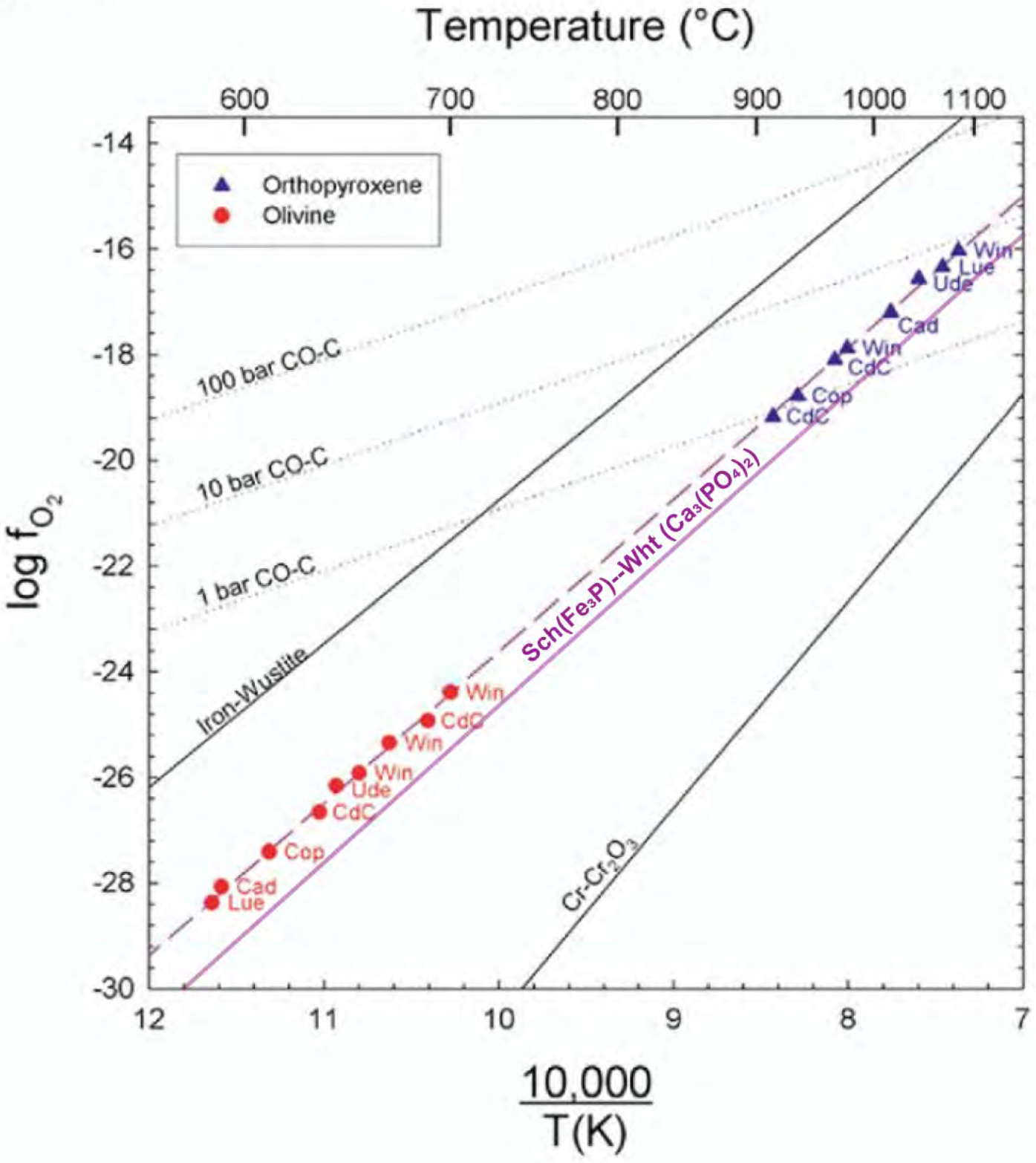

Always consult and cite the final, published document. See http:/www.minsocam.org or GeoscienceWorld

This is the peer-reviewed, final accepted version for American Mineralogist, published by the Mineralogical Society of America.
The published version is subject to change. Cite as Authors (Year) Title. American Mineralogist, in press.
DOI: https://doi.org/10.2138/am-2023-9195. http://www.minsocam.org/

Figure 6

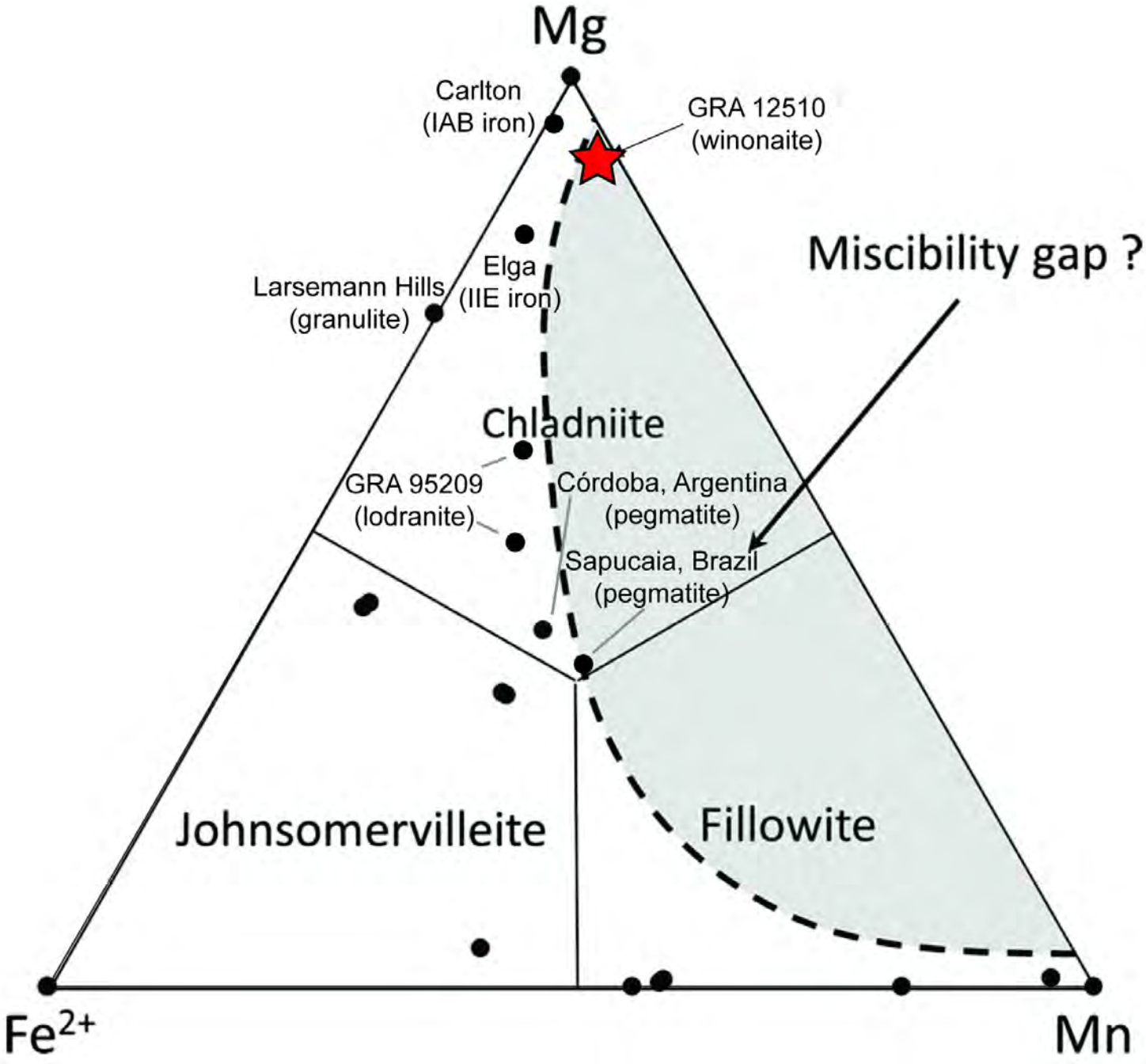

Always consult and cite the final, published document. See http:/www.minsocam.org or GeoscienceWorld